MOLECULAR DYNAMICS SIMULATION OF AL EXPLOSIVE BOILING AND TRANSCRITICAL REGIMES IN NANOSECOND LASER ABLATION

A.A. SAMOKHIN[1], V.I. MAZHUKIN[2,3], M.M. DEMIN[2], A.V. SHAPRANOV[2,3], A.E. ZUBKO[1]

[1] A.M. Prokhorov General Physics Institute, RAS, Moscow, Russia
e-mail: asam40@mail.ru, web page: http://www.gpi.ru/eng/

[2] Keldysh Institute of Applied Mathematics, RAS, Moscow, Russia
e-mail: vim@modhef.ru, web page: http://www.keldysh.ru/

[3] National Research Nuclear University "MEPhI", Moscow, Russia
web page: https://mephi.ru/eng/

Summary. Recoil pressure behavior during nanosecond laser ablation of thin (450 nm) Al liquid film is analyzed on the basis of molecular dynamics calculations. It is shown that the recoil pressure demonstrates appearance and disappearance of repeating pressure peaks due to explosive boiling at some range of constant laser intensity and nanosecond durations of irradiation which is switched on at $t = 0$. This effect can be used as a marker for approach of liquid-vapor critical point. Some other nonequilibrium features of near-critical laser ablation are also discussed.

1 INTRODUCTION

In recent years laser ablation process is intensively investigated for the case of short (femtosecond) pulses of radiation [1-2], while nanosecond ablation remains less investigated. In particular, there is no sufficient theoretical and experimental information on near-critical irradiated matter behavior including explosive boiling process in metastable liquids near its superheating limit. Such information is necessary *e.g.*, for experimental determination of metal critical parameters which as a rule cannot be measured within the usual steady-state approaches except for only few metals like Hg and Cs with sufficiently low pressure and temperature values at critical point of liquid–vapor phase transition. However, recoil pressure time behavior in nanosecond laser ablation regime has not been analyzed yet theoretically and experimentally.

The problem of poor information about metal critical parameters is clearly mentioned in various papers (see e.g. [3-4]) and is evident as well from significant variations of critical parameters estimations for the same metal [1, 3]. It should be mentioned also that up to now there is no sufficient experimental and theoretical information on critical parameters manifestations in non-equilibrium conditions of nanosecond laser ablation.

In the present paper nanosecond laser ablation of thin liquid Al films is analyzed in the basis of molecular dynamic (MD) modeling [5-6] which is up to now the most effective approach to describe strongly non-equilibrium behavior of superheated matter. This behavior could not be considered in the framework of usual continual (hydrodynamic) or kinetic approaches.

2010 Mathematics Subject Classification: 82D15, 82D35, 82D80.
Key words and Phrases: Molecular dynamics, nanosecond laser ablation, explosive boiling, critical point.

In the nanosecond laser ablation regime there is a possibility to observe repeated pressure peaks due to explosive boiling which can be used as markers for attaining near-critical region (see e.g. [6] and references therein). Such repeated peaks can be hardly observed during and after short (picosecond or shorter) laser pulse action. Some of these results were presented in COLA 2017 conference [7].

2 STATEMENT OF THE PROBLEM

The statement of the problem and modeling parameters are described in [8] and briefly repeated here. Some details are also given in appendices 1-3, in particular, about temperature and density distributions along the Z and Y axis as well as initial state preparation and calculation of equilibrium states parameters.

As it is already mentioned in the abstract and introduction the main purpose of our investigation relates to the recoil pressure behavior during nanosecond irradiation of liquid metal (Al) film in the framework of molecular dynamic simulation.

The metal film is considered as a combination of two interacting subsystems consisting respectively of the conduction electrons and the lattice ions with energy exchange between them [9-11]. This means that in general the subsystems are not in equilibrium with each other, for example, they may have different temperatures at the same point in space. Such an approach has been proposed previously to describe the spin systems in solids [12], the electronic and ionic subsystems in gas plasma [13].

Laser radiation propagates from right to left and is normally incident on the free surface of the film. Part of the radiation is absorbed by the electronic components, and as a result of inelastic collisions is transferred to the ion subsystem. In the present paper, electron temperature diffusion is considered in one-dimensional approximation (along the Z direction). Justification of this approximation to some degree can be realized by comparison of temperature distributions along the Z and Y directions which is considered in appendix 3. One can see that these distributions are very similar though no electron temperature diffusion along Y direction is taken into account. It seems probable that in such a case allowance for electron temperature diffusion in Y direction is not among urgent needs except for strongly inhomogeneous ablation plume region.

Combined TTM–MD (Two Temperature Model – Molecular Dynamics) [8,14] is used to describe the processes. It should be mentioned that in the considered ablation regime electron and ion (lattice) temperatures differ but slightly and the main effect of the two-temperature model is in introducing electron heat conductivity which exceeds the lattice conductivity by orders of magnitude.

Energy balance of electron subsystem is described by continuum energy equation (1) supplemented by the equation of laser radiation transfer (2):

$$\frac{\partial \varepsilon_e}{\partial t} = -\left(\frac{\partial W_e}{\partial z} + g(T_e)(T_e - T_i) + \frac{\partial G}{\partial z}\right) \tag{1}$$

$$\frac{\partial G}{\partial z} + \alpha G = 0 \tag{2}$$

Here $\varepsilon_e = \varepsilon_e(N_e, T_e) = \int_0^{T_e} C_e(N_e, T_e) dT_e$ is the volume density of electron energy, C_e is specific heat of the electron Fermi gas, N_e is electron density, T_e, T_i are the electron and ion temperatures, $g(T_e)$ is the electron-ion coupling coefficient, G is the density of laser radiation

flux in the medium, $\alpha = \alpha(T_e, n_e)$ is the coefficient of absorption of laser radiation, $W_e = -\lambda_e \partial T_e / \partial x$ is the heat flux, $\lambda_e(T_e, T_i)$ is the electron heat conductivity coefficient.

The energy balance equation of the electron subsystem (1) was solved in the condensed medium using the finite-difference method. Zero heat flux $W_e = 0$ was used as a boundary condition at the surface of the film and its fragments.

The connection between electron energy and temperature was obtained using approximation via Fermi integrals [15].

3D molecular-dynamic modeling was used to describe the ion motion:

$$\begin{cases} \dfrac{d\vec{r}_j}{dt} = \vec{v}_j \\ m_j \dfrac{d\vec{v}_j}{dt} = \vec{F}_j^{emb} + \vec{F}_j^{heat} \end{cases} \qquad j = 1..N \tag{3}$$

Here m_j, $\vec{r}_j$, $\vec{v}_j$ are the mass, radius-vector and velocity of j-th ion respectively, $\vec{F}_j^{emb} = -\partial U(\vec{r}_1 \ldots \vec{r}_N)/\partial \vec{r}_j$ is the force acting at the j-th ion from other ions, $U(\vec{r}_1 \ldots \vec{r}_N)$ is the interaction potential for which embedded atom model (EAM) potential for Al [16] was chosen (see appendix 2). The energy transfer from the electron subsystem to the ion is given by:

$$\vec{F}_j^{heat} = \frac{m_j(\vec{v}_j - \langle \vec{v} \rangle)}{3k_B T_i n_i} g(T_e)(T_e - T_i) \tag{4}$$

where $\langle \vec{v} \rangle$ is the mean ion velocity in the neighborhood of the j-th ion. The calculation procedure provides the total energy conservation with the accuracy better than 10^{-7}.

The values of the coefficients $g(T_e)$, $C_e(T_e)$ and $\lambda_e(T_e, T_i)$ are given in [8]. For example at $T_e = 7000$ K for C_e and g one has respectively 6×10^5 J/m^{3}K and 2.5×10^{17} W/m^{3}K which give for the relaxation time $\tau = C_e/g$ is about 2 ps or smaller if lattice heating is taken into account.

Critical parameters for the considered Al model are $T_C = 7600$ K, $P_C = 1400$ bar, $\rho_C = 0.5$ g/cm^3. Various different critical parameter values for Al and other metals are given in ref. [1, 3]. It should be stressed that the real experimental values of the critical parameters for Al are not known and its absolute values given above should be considered only as a result of the model used. Nevertheless it is supposed that this fact is not very important for obtaining new information on non-equilibrium behavior of the system under consideration described with the help of reduced parameters.

At the initial time $t = 0$ the film was assumed to be heated to the temperature of 6340 K, electron and ion subsystems are in thermal equilibrium. The state preparation is described in appendix 2. Initial pressure values $P = 0$ gives rise to acoustical film vibrations which are discussed in [5]. The initial sample dimensions are $L_x \times L_y \times L_z = 37.3\times37.3\times449$ nm^3 with the total particle number $N = 17.87\times10^6$ and periodical boundary conditions along X–Y directions.

3 RESULTS AND DISCUSSION

3.1 Time evolution of pressure recoil $P(t)$ and phase trajectories in P-T, P-ρ, T-ρ planes at different ablation regimes

Fig. 1 shows recoil pressure and surface temperature behavior at different constant

radiation intensity $I = 33$, 44, 66 and 110 MW/cm^2 which are switched on at $t = 0$. For the cases with sufficiently sharp liquid-vapor boundary the recoil pressure means the pressure value in liquid layer adjacent to the evaporating front with the distance $\Delta z = 8$ nm from it. It should be mentioned that sharp liquid-vapor front width when the density drop far below the critical density ρ_c is about 3 nm. At higher temperature when the liquid-vapor density jump is not pronounced the pressure and temperature values are taken at the point $z_b = z_c - \Delta z$ where z_c is determined by the relation $\rho(z_c) = \rho_c$ for the sake of convenience.

The pressure peaks on curves 1, 2 in fig. 1a are due to explosive boiling process which begins to develop when the superheating limit temperature is attained in the irradiated liquid. Initial ablation stage (before the explosive boiling) corresponds to the surface evaporation regime which is considered in some details in section 3.3. At not very high intensity after the first explosion is over the system returns almost to same states as before the explosion and then the process is repeated. It is clear that at higher laser intensity which provides faster heating rate such repeated explosive boiling process can not be realized because after the first explosion the system attains unstable (labile) or even supercritical states. Theoretical and experimental investigations of such regimes can give new information on non-equilibrium behavior of irradiated metals in its near-critical states.

It should be mentioned that the explosive boiling process in the considered case differs markedly from the process of generation and evolution of separate vapor spherical bubbles at small superheating levels [12]. At high superheating many vapor nucleus appear almost simultaneously which can not be considered as independent and isolated. Moreover near the evaporating surface where nucleation occurs one should take into account time-dependent temperature gradients and their effect on the formation and evolution of vapor cavity which differs from simple spherical bubble. For these reasons it is not convenient to consider the case of strong superheating in terms which are appropriate to small superheating picture.

Fig. 1b shows recoil pressure P (curve 1) and temperature T (curve 2) behavior of the left side of the film which is heated due to metal (electron) thermal conductivity. Remarkably that the explosive boiling occurs also in the left film side where T corresponds the lowest value in the film temperature distribution. Possibility of such explosion is due to the fact that the pressure also has the lowest value in this region.

Maximum pressure value during explosive boiling is somewhat lower than saturated pressure value $P_S(T)$ at temperature T just before the explosive boiling begins. This is valid for all the cases considered here and it is illustrated with curve 2 in fig. 1b which describes the saturated pressure and temperature behavior on the left film side. In the considered interval $\Delta P \approx (\partial P/\partial T)\, \Delta T$ so that the saturated pressure and temperature behavior can be represented with the same curve 2.

The surface film temperature at the explosive boiling beginning depends on the recoil pressure value and increases with growing pressure. In some cases this dependence can be considered as non-equilibrium analog to spinodal line in continuous equation of state (EoS) *e.g.*, Van der Waals equation (VdW).

The pressure rise during the first explosive boiling for $I = 33$ MW/cm^2 begins at $t = 1.5$ ns and $T = 6900$ K. The explosive boiling development leads to some temperature decreasing of the temperature value which is clearly seen for the curve 3 in fig. 1a. It is worthwhile to remind here that according to VdW-like EoS in superheated metastable liquid the heat capacity C_P diverges and changes it sign at the spinodal line.

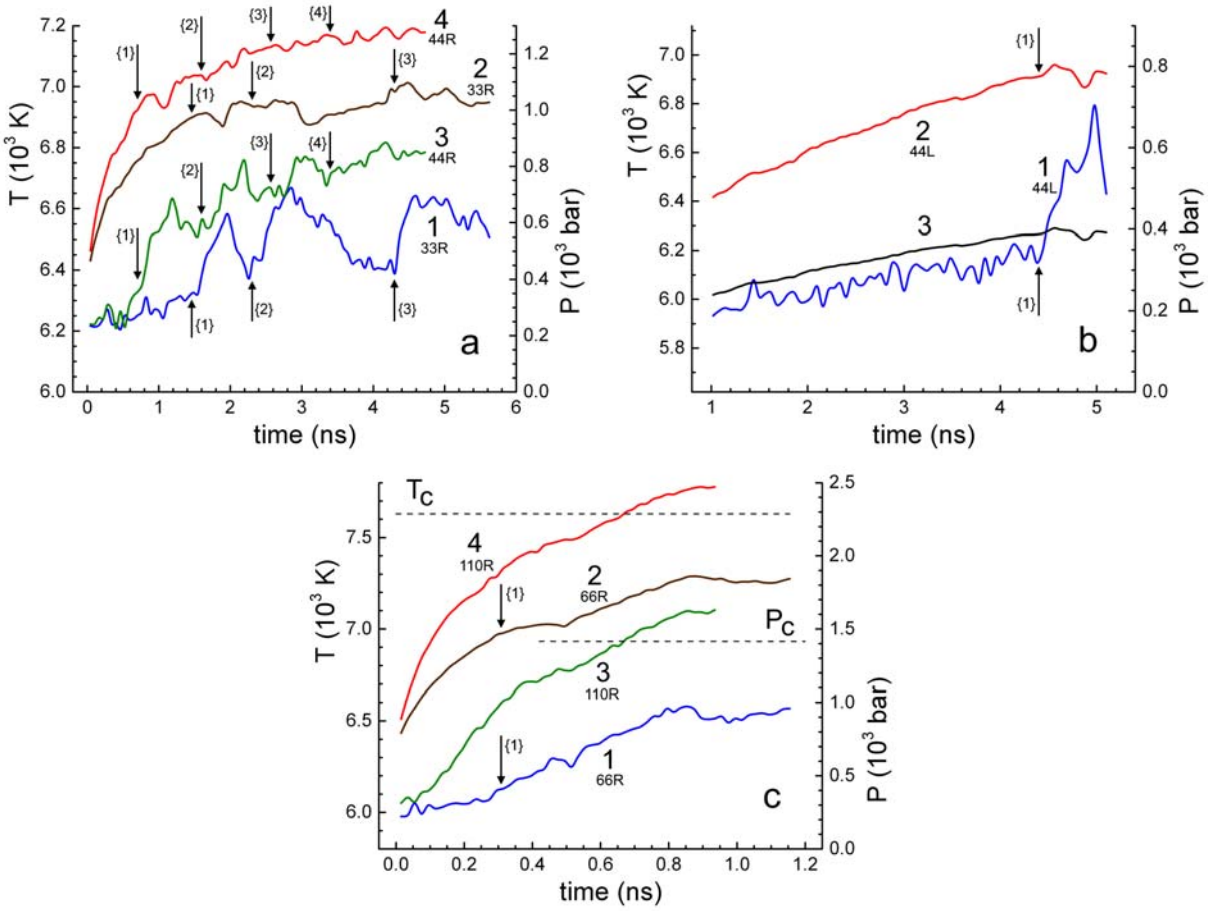

Fig. 1. Pressure (curves a1, a3, c1, c3) and temperature (a2, a4, c2, c4) behavior on the irradiated (R, right) surface of liquid Al film at different constant radiation intensity I = 33 (a1, a2); 44 (a3, a4); 66 (c1, c2); 110 (c3, c4) MW/cm^2 switched on at t = 0. Pressure (b1) and temperature (b2) behavior together with saturated pressure $P_S(T)$ (curve b2) and $P_S(T)/2$ (curve b3) on the film left (L) surface at I = 44 MW/cm^2. The arrows indicate the time just before the explosive boiling begins and its successive number is given in braces.

The explosive boiling pressure peaks are more pronounced at lower intensity as one can see from comparison of curves 1, 2 in fig. 1a. It should be noted that for $I = 44$ MW/cm^2 the pressure peaks become rather small after $t > 4$ ns with mean recoil pressure $P = 850$ bar $= 0.6\, P_C$. Such pressure peaks disappear also at higher intensity as it is shown in fig. 1c for $I = 66$ and 110 MW/cm^2. At higher heating rates which are realized for $I = 66$ and 110 MW/cm^2 there is no sufficient time for the explosive boiling process to develop.

Additional features of the system behavior can be illustrated with the help of its pathways on different thermodynamic planes. The points on the P–T plane which correspond to the system states just before the first and successive explosive boiling beginning are shown in fig. 2a together with binodal $P_S(T)$ (curve 2).

The superheating limit line determined by the point positions can be associated with the spinodal (curve 1) in EoS mentioned above. The states between curves 2 and 1 and below 1 are, respectively, metastable and labile.

Fig. 2b-d demonstrates the phase trajectories (curves 1-5) in P-T, P-ρ, T-ρ planes

respectively at different irradiation intensities: 33 MW/cm^2 (curve 1), 44 (2-3), 66 (4), 110 (5). The curve 2 corresponds to the left side of the film while the other curves (1,3-5) belong to its right side. The curve 6 describes the binodal line with calculated critical point T_C = 7600 K, P_C = 1400 bar, ρ_C = 0.5 g/cm^3.

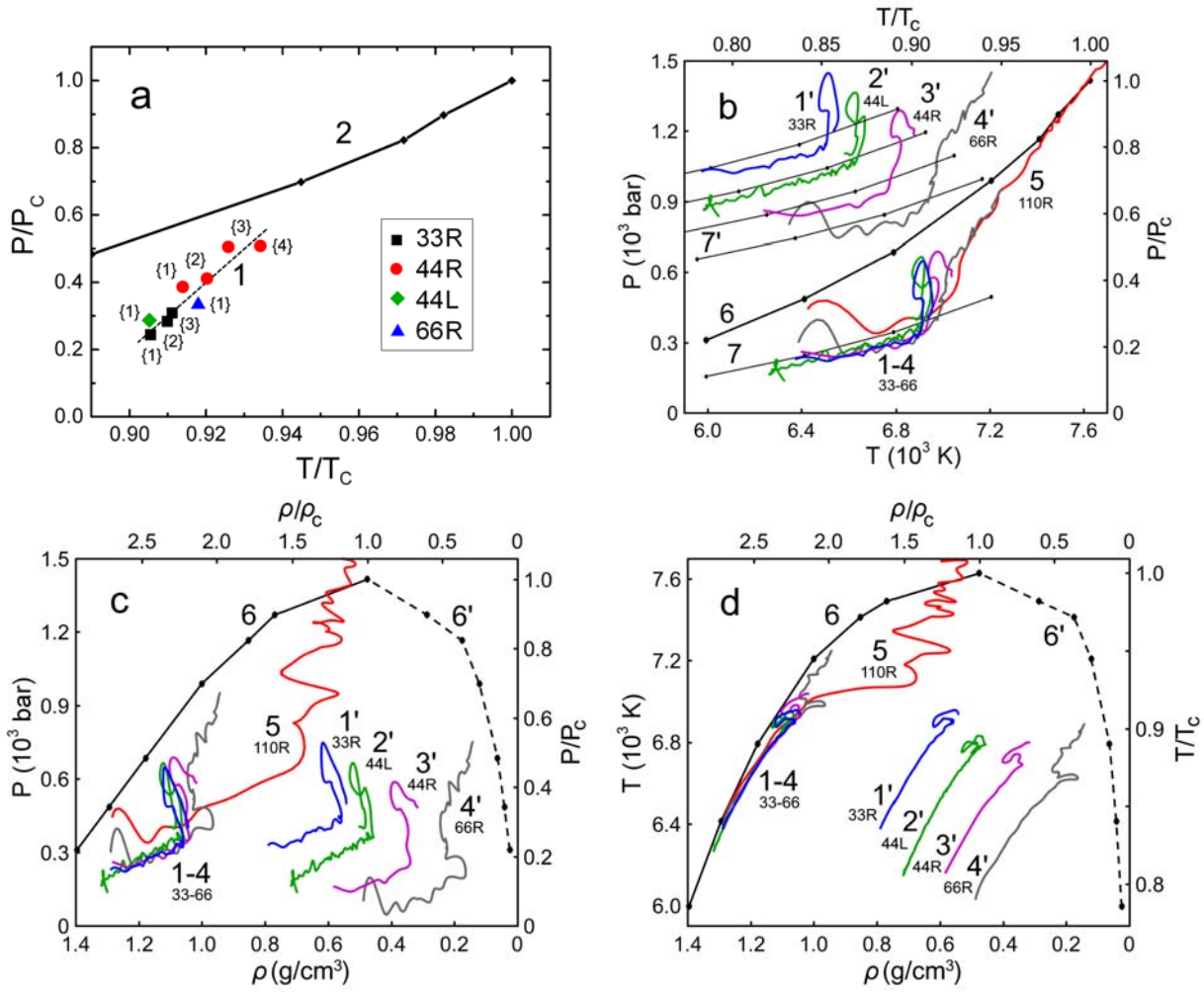

Fig. 2. **a**: Pressure and temperature values at the moment of the explosive boiling beginning at different heating condition (33, 44, 66 MW/cm^2) at right (R) and left (L) film sides. The number in braces indicate the successive explosive boiling; **b-d**: Irradiated system pathways in P-T, P-ρ, T-ρ planes respectively at different heating condition 33 (curve 1), 44 (2, left film side), 44 (3), 66 (4), 110 (5) MW/cm^2. Curves 1′-4′ are displaced from its original positions 1-4 (see the text) for the observation convenience. Curve 2 in **a** and 6 in **b-d** describe the binodal line. Curve 7 and four smooth curves (7′) represents the $P_S(T)/2$ line in its original and four displaced positions.

All considered trajectories except for the curve 5 are rather close to each other so it is difficult enough to follow its individual behavior. For this reason, in fig. 2b-d the curves 1-4 and part of curve 7 are also presented separately (1′-4′, (7′)) with some displacement relatively to its original positions (1-4,7). For curve 1′ the displacements are 800 bar and 400 K in fig. 2b; 100 bar and 0.5 g/cm^3 in fig. 2c,d. For curves 2′-4′ the periodic displacements are 120 K, 0.1 g/cm^3 and 100 bar relatively to curve 1′.

The system parameters are taken at some subsurface point z_b which corresponds to the superheated liquid state as it was already mentioned in the beginning of the section. The distance between z_b and the surface is $\Delta z = 8$ nm. After the explosive boiling process begins and the subsurface density drops at the level of $0.9\rho_b$ compared with its value ρ_b just before the explosion, the point z_b is displaced at the new position determined by the new vaporization front location. This displacement does not give rise to appreciable changes in considered parameters due to their relatively smooth behavior.

The system trajectories in P-T plane (fig. 2b) lie below binodal line (curve 6), i.e. in metastable region which corresponds to superheated liquid state. This metastability is mainly due to the fact that the liquid pressure P at given temperature T is lower than its saturated pressure $P_S(T)$ described as the binodal line in fig. 2b.

In the free surface evaporation case (before the explosive boiling) the trajectories, except for their initial parts, lie even somewhat below $P_S(T)/2$ line (curve 7) which is the minimum value of pressure recoil [12] for evaporation model where vapor is considered as an ideal gas. Reasons for this difference are briefly discussed in section 3.3.

Further evolution of the trajectories in fig. 2b is determined by the explosive boiling process when the pressure grows up to the level $0.85P_S(T)$ almost at the constant temperature T and then begin to diminish remaining above $P_S(T)/2$ level (curves 1-3). At $I = 66$ and 110 MW/cm^2 (curves 4-5) there is no such diminishment and the pressure growth is not so sharp. In the case of $I = 110$ MW/cm^2 (curve 5) the system finally exits two-phase region as it is seen also in fig. 2c-d.

The curves 1′-4′ in fig. 2c are similar to their counterparts in fig. 2b while in fig. 2d explosive boiling effect is less pronounced than in fig. 2b-c. This difference is due to the fact that in this process relative temperature and density changes in liquid phase are smaller that the corresponding pressure changes.

It is necessary to mention that the evolution times t_i along the considered trajectories are different. For the curves 1-5 in fig. 2b-d one has $t_i = 2200$ ps, 5400 ps, 1450 ps, 400 ps, 1150 ps respectively. In the cases 1-4 the first explosive boiling occurs at 1600 ps, 4500 ps, 800 ps, 300 ps respectively while in the case 5 the system reaches critical point at 650 ps and temperature level $0.94T_C$ at 200 ps. The relative values of the calculated time intervals give grounds to suppose that at higher intensities there is no sufficient time for explosive boiling development in the superheated metastable liquid.

It should be mentioned that at higher intensities and shorter laser pulses instead of explosive boiling the spallation effect is observed which is initiated, in particular, with negative pressure values induced in irradiated matter [4]. In contrast to the spallation explosive boiling begins when initial pressure value is positive. In some cases, probably after the short laser pulse action explosive boiling can also develop provided the sample temperature remains sufficiently high. However, after the short laser pulses in strongly absorbing matter appearance of repetitive explosive boilings such as in fig. 1a is scarcely possible and has not been observed theoretically or experimentally up to now.

Film parameters distributions at different times during explosion boiling and other ablation regimes are discussed in the following section.

3.2 Space distributions of P, T, ρ, V_Z at different times and intensities

Film displacement to the left at fig. 3-6(a) is due to its real movement because of the

pressure difference on its right and left sides while the curve shifts in fig. 3-6(bcde) are made for the presentation convenience. The right hand side curve displacements are different from its left counterparts due to ablation process. The right-left sides recoil pressure difference is clearly seen in fig. 3d where also the maximum pressure growth from 330 bar to 600 bar during the phase explosion is also visible.

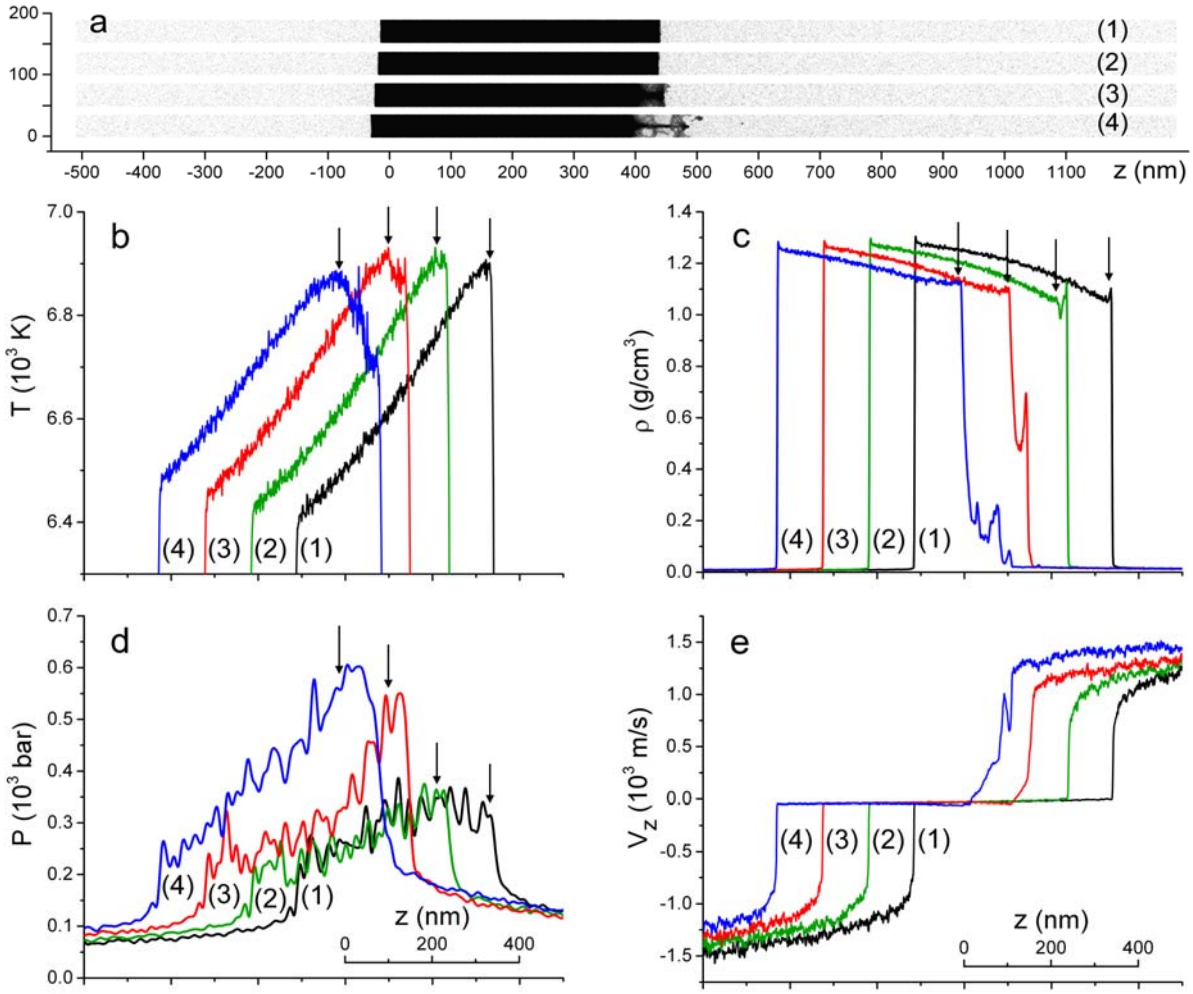

Fig. 3. 2D particle distribution in Y–Z plane (a), 1D space distribution of temperature T (b), density ρ (c), pressure P (d) and mean velocity V_Z (e) at t = 1440 (curves 1), 1560 (2), 1740 (3), 1905 (4) ps before and during the first explosive boiling for I = 33 MW/cm^2. The arrows show some points in the liquid which are used for pathways construction in fig. 2b-d as well as P(t) and T(t) curves in fig. 1. The space scale in b,c is the same as in d,e.

The explosive boiling development leads to the flattening of the temperature distribution near its maximum (curve 2, fig. 3b) and subsequent temperature diminishing (curves 3, 4) near the right side of the film. The temperature drop is also visible in curve 2, fig. 1a at $t \approx 1.7$ ns when the first explosion begins. For $I = 44$ MW/cm^2 the same temperature behavior is observed at $t \approx 1$ ns.

Changing of the mean particle velocity V_Z and the film density during the explosion are demonstrated in fig. 3e,c. Due to explosive boiling fragmentation process the velocity and

density distributions (curves 3,4 in fig. 3c,e) at the film right hand side become wider and non-monotonous as compared to the surface evaporation case described with curves 1, 2. Investigation of the vapor-droplet flow in various ablation regimes is out of the present paper scope. Surface evaporation cooling leads to the appearance of the subsurface temperature maximum and the corresponding surface density pip (curves 1, 2 in fig. 3b,c).

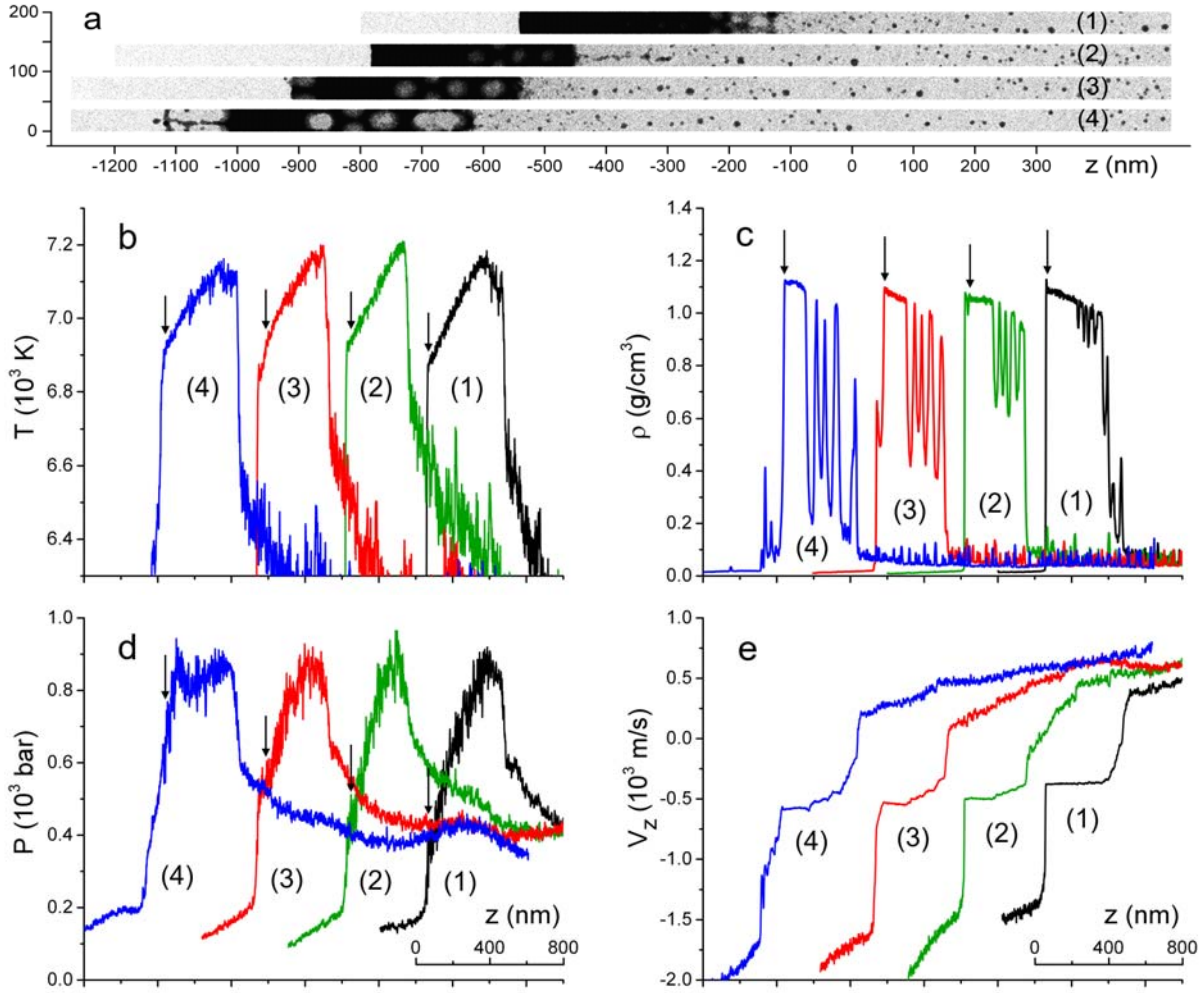

Fig. 4. 2D particle distribution in Y–Z plane (a), 1D space distribution of temperature T (b), density ρ (c), pressure P (d) and mean velocity V_Z (e) at t = 3945 (curves 1), 4515 (2), 4740 (3), 4995 (4) ps during explosive boiling and spinodal decomposition for I = 44 MW/cm^2. The arrows show some points in the liquid which are used for pathways construction in fig. 2b-d as well as P(t) and T(t) curves in fig. 1. The space scale in b,c is the same as in d,e.

For $I = 44$ MW/cm^2 the film displacement due to recoil pressure difference is more pronounced as it is seen from fig. 4a. The fig. 4a also demonstrate the ablation regime which follows after the explosive boiling and can be associated with spinodal decomposition. Effect of spinodal decomposition on density distribution is demonstrated in fig. 4c. There is no recoil pressure growth in this regime as it is seen from fig. 4d and fig. 1. The spinodal decomposition gives rise to small effect on the temperature distribution (fig. 4b) or time behavior (curve 4, fig. 1a).

The left side of the curves 2-4 in fig. 4c-e shows the explosive boiling development on the left film side which begins at $T = 6910$ K and $P = 400$ bar. This point corresponds to the lowest temperature and pressure values in the film and is close to superheating limit temperature or spinodal line in fig. 2a.

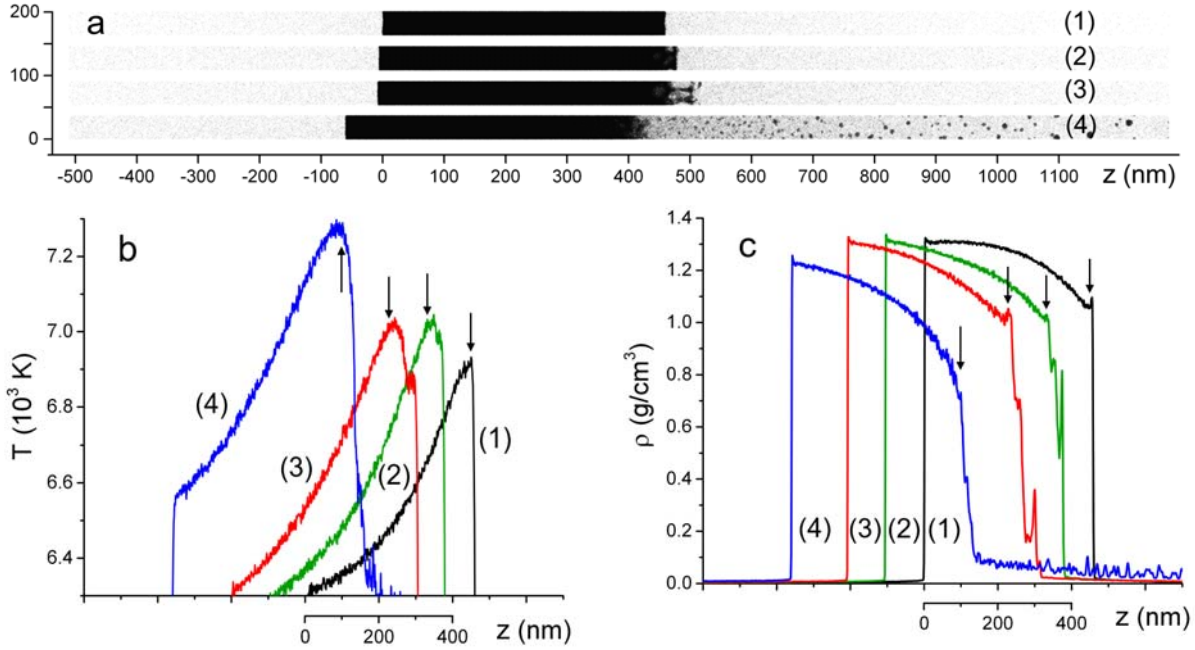

Fig. 5. 2D particle distribution in Y–Z plane (a), 1D space distribution of temperature T (b) and density ρ (c) at t = 250 (curves 1), 415 (2), 490 (3), 1155 (4) ps for I = 66 MW/cm^2. The arrows show some points in the liquid which are used for pathways construction in fig. 2b-d as well as P(t) and T(t) curves in fig. 1.

For $I = 66$ MW/cm^2 one can observe only one explosion at $t = 415$ ps with rather small pressure rise. The explosive boiling effect is also visible on the temperature (curve 3) and density (curves 2, 3) distributions in fig. 5. At the P–T plane in fig. 2 the process beginning corresponds to the point "66R". At $t > 500$ ps the curves $P(t)$ and $T(t)$ (fig. 1c) as well as temperature and density distributions (fig. 5) have no peculiarities which can be attributed to the explosive boiling or spinodal decomposition processes. One can see from snapshot and density distribution that at this time the film state is subcritical though the liquid-vapor phase transition front becomes rather smooth and wider in contrast to the moments at $t < 400$ ps. In particular, there is no density peak (curve 4, fig. 5c) due to surface evaporating cooling which is clearly visible at curves 1-3.

At $I = 110$ MW/cm^2 the time behavior of pressure and temperature are smooth as well as 2D particle distribution, $\rho(z)$ and $T(z)$ (fig. 1, 6). In this case sharp liquid-vapor front transition disappears at early times $t > 200$ ps so that temporal behavior of $P(z_b, t)$ and $T(z_b, t)$ refer to the point $z_b = z_c - \Delta z$ where $\Delta z = 8$ *nm* and $\rho(z_c, t) = \rho_c$. The film parameters $P(t) > P_C$ and $T(t) > T_C$ become supercritical at $t > 670$ ps with no explicit manifestation of any singularities during critical point passing.

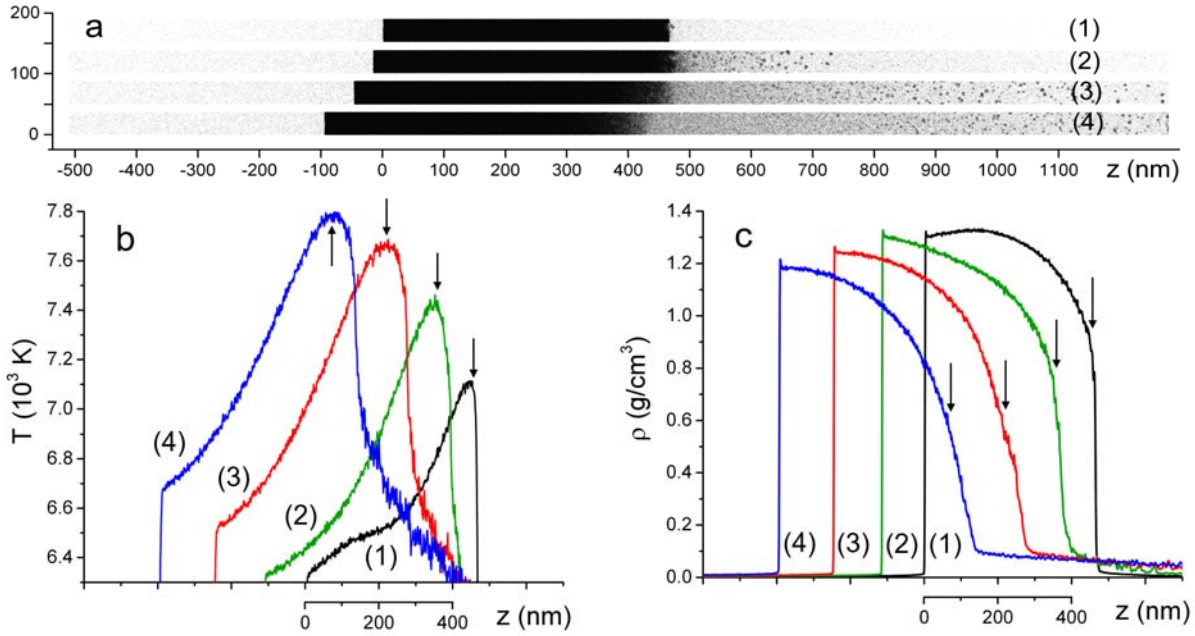

Fig. 6. 2D particle distribution in Y–Z plane (a), 1D space distribution of temperature T (b) and density ρ (c) at t = 170 (curves 1), 400 (2), 700 (3), 950 (4) ps for I = 110 MW/cm^2. The arrows show some points in the liquid which are used for pathways construction in fig. 2b-d as well as P(t) and T(t) curves in fig. 1.

3.3 Surface evaporation regime: comparison with simple kinetic and hydrodynamic approaches

For not very intensive surface evaporation into vacuum and the mass accommodation coefficient a_m=1 the evaporating mass flow can be approximated with well-known Hertz–Knudsen (HK) relation [12]

$$j_\rho = \rho_S \sqrt{\frac{kT_S}{2\pi m_0}} \tag{5}$$

$$j_P = P_S \sqrt{\frac{m_0}{2\pi kT_S}} \tag{6}$$

$$j = \rho V \tag{7}$$

The two equations (5), (6) are equivalent for ideal gas with equation of state $P_S=(\rho_S/m_0)kT_S$ where P_S, ρ_S, m_0, T_S are the saturated vapor pressure, density, particle mass and evaporating surface temperature. The net vapor flow is somewhat lower compared to equations (5), (6) due to backscattering process (see e.g. [17], and references therein).

The vapor flow values obtained in our calculation at different times and intensity: t = 3945 ps (No 1, left) and 600 ps (No 2) and I = 44 MW/cm^2; t = 1440 ps and I = 33 MW/cm^2 (No 3); t = 250 ps and I = 66 MW/cm^2 (No 4) are shown in table 1 together with corresponding values given by equation (5), (6) at the same surface temperature,

saturated vapor pressure and density values.

№	T, K	ρ, g/cm^3	P, bar	j_ρ, g/(cm^{2}s)	j_P, g/(cm^{2}s)	j, g/(cm^{2}s)
1	6870	0.0740	740	4290	2050	1670
2	6880	0.0752	751	4370	2080	1700
3	6900	0.0780	765	4540	2120	1700
4	6920	0.0808	780	4710	2160	1710

Table 1. Comparison of vapor flow values calculated from in the modeling (j) and two forms of HK relation (j_ρ, j_P) corresponding to equation (5), (6).

From the table 1 it follows that the expressions for the mass flow (5), (6) which are equivalent for ideal gas differ significantly in more general case. This difference is due to EoS deviation in the considered case from ideal gas EoS. From the two relations (5), (6) the first is closer to MD calculation results for mass flow.

It is interesting to note that the recoil pressure in fig. 1b before the explosive boiling is slightly lower than $P_S(T)/2$. This difference can be probably attributed to the mass accommodation coefficient value $a_m<1$ [17], non-ideal gas effects in vapor flow or finite relaxation times in formation of the surface evaporation flow. However, the situation needs further investigation which is out of the present paper scope devoted mainly to explosive boiling and spinodal decomposition of superheated metastable liquid.

4 CONCLUSIONS

Our results show that in nanosecond laser ablation repeating explosive boilings occur at some values of laser intensities and irradiation times which give rise to repeating peaks appearance in recoil pressure behavior. Such recoil pressure peaks can be used as markers for attaining near-critical region in superheated metastable liquids as it was supposed long ago in [18]. No explosive boiling is observed at mean recoil pressure level above approximately $P_l \approx 0.6\, P_C$. Possible correlation between P_l and P_C needs further investigations for different laser pulse, metals and models. It is interesting also to investigate experimentally the recoil pressure behavior for metal with known critical parameters, *e.g.* for Hg.

It should be mentioned that ablation regime can be affected with plasma formation which is not considered here. Appearance of strongly absorbing plasma layer can change non-equilibrium properties of vaporization process. In the case of free vapor expansion into vacuum the corresponding mass flow has its maximum value which can be diminished because of expansion limitation due to plasma formation [19-22]. The vaporization rate during laser ablation can be investigated experimentally with the acoustical monitoring method [23-24].

Acknowledgements: The research was funded by the Russian Foundation for Basic Research, grant No 16-07-00263.

APPENDIX 1. PERIODIC BOUNDARY CONDITIONS AND INITIAL STATE PREPARATION.

Suppose that the aim of the simulation is to study the laser heating of a thin metal film of thickness H in a vacuum. The film is formed by a set of particles located at the nodes of the crystal lattice. For modeling, a finite computational domain is chosen with the dimensions along the axes $L_x \times L_y \times L_z$, which contains part of the film $L_x \times L_y \times H$ (Fig. a1). Thus, in the direction of the coordinate axes X and Y, the film is infinite, and the computational domain is finite. To model the interaction with the part not included in the computational domain, periodic boundary conditions are used along the axes X and Y with the periods L_x and L_y respectively.

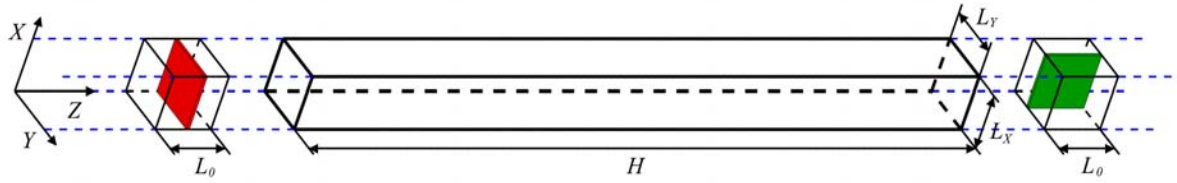

Fig.a1. Computational domain for modeling of the infinite film with periodic boundary condition along X–Y axes and period $L_x = L_y = L_0 = 37.3$ nm. Initial film thickness H(t=0) = 449 nm and the total length of computation domain $L_z = 2$ μm. Parts marked with L_0 are explained in appendix 3.

Periodic boundary conditions along x imply that the particles, which x coordinate is within the interval $0 \le x < L_x$, exactly reproduce the particles $kL_x \le x < (k+1)L_x$ for any integer $k \neq 0$. That is, the particle leaving the computational domain from the upper boundary $x = L_x$, is replaced by the particle with the same value of velocity but entering the computational domain through the bottom boundary $x = 0$. If we mark the quantities related to a new particle with a stroke, then

$$\begin{cases} \vec{v}' = \vec{v} \\ x' = (x - L_x) \in [0, L_x) \quad for \quad L_x \le x < 2L_x \\ y' = y \\ z' = z \end{cases} \tag{a1.1a}$$

Similarly, for a particle leaving the computational region through the bottom boundary $x = 0$:

$$\begin{cases} \vec{v}' = \vec{v} \\ x' = (x + L_x) \in [0, L_x) \quad for \quad -L_x \le x < 0 \\ y' = y \\ z' = z \end{cases} \tag{a1.1b}$$

The second important aspect of periodic boundary conditions is the force and potential energy of interaction for particles from the border regions: $0 \le x < r_{cr}$ and $(L_x - r_{cr}) \le x < L_x$, where r_{cr} is the cutoff radius of the potential (it is supposed that the interaction force can be neglected at the distances $r > r_{cr}$).

The interaction of the particle i, which coordinate x_i is within the interval $(L_x - r_{cr}) \le x_i < L_x$ with the particles beyond the computational region $L_x \le x_j' < (L_x + r_{cr})$ is modeled using the particles $0 \le x_j < r_{cr}$ from the computational domain, the radius-vectors of which are adjusted

in the following way during the calculation of force $\vec{F}_{ij} = \vec{F}_{\left(\ldots\vec{r}'_j\ldots\right)}(\vec{r}_i)$:

$$\vec{r}'_j = \vec{r}_j + \vec{e}_x L_x \tag{a1.2}$$

where $\vec{e}_x$ is the single unit axis of the axis *X*.

Obviously, all of the foregoing applies equally to periodic boundary conditions along the coordinate axis *Y*.

The question of the error introduced by periodic boundary conditions is due to the distortion introduced into the damping of the phonon modes in the crystal. Obviously, expanding the boundaries reduces the effect on the spectrum of the phonon modes.

In the direction of the *Z* axis, the film is finite and its surfaces are free from external influences (with the exception of heating by an external energy source). Therefore, no special boundary conditions in this direction are required. Boundaries at the ends of computational domain L_z are completely transparent.

The heating of the target in the range of 300 K – 6400 K was performed by the Berendsen thermostat [25] with enabled Berendsen barostat with zero target pressure [26]. The temperature of 6400 K was reached within $t \sim 200$ ps. After that, the thermostat and barostat were turned off and were replaced by the laser pulse heating with constant intensity.

APPENDIX 2. THE POTENTIAL OF THE EMBEDDED ATOM MODEL (EAM).

In the 80s of the last century, an approach was proposed to the description of energy states applicable to compounds with a metal bond [27, 28]. Based on the idea of the quantum-mechanical theory of the electron density functional, the contribution to the energy of arbitrarily located nuclei from interaction with electrons can be written as a single-valued functional of the total electron density (the embedding functional). In this case, the total electron density in the metal is represented as a linear superposition of the contributions of individual atoms, and the electron density created by one atom is spherically symmetric. Thus, the total energy of the system consists of two terms: the energy of pair interaction of atoms and the energy of interaction of each atom with the electron density created by other atoms:

$$U(\overrightarrow{r_1}\ldots\overrightarrow{r_N}) = \frac{1}{2}\sum_{\substack{i,j=1\\ i\neq j}}^{N}\varphi(r_{ij}) + \sum_{i=1}^{N} f(\rho_i) \tag{a2.1a}$$

where $\varphi(r_{ij})$ is the pair potential, $f(\rho_i)$ is the embedding function of the *i*-th atom, ρ_i is the total electron density for the *i*-th atom, produced by spherically symmetric functions of single-electron density $n(r_{ij})$ of other atoms:

$$\rho_i = \sum_{\substack{j=1\\ j\neq i}}^{N} n(r_{ij}) \tag{a2.1b}$$

This approach was named the embedded atom model (EAM) and the expressions (a2.1) were named the EAM potential.

In some cases, one try to calculate the functions $\varphi(r)$, $n(r)$, $f(\rho)$ on the basis of the

quantum-mechanical theory. In most cases, different approximating formulas are chosen with parameters whose values are adjusted to the experimental values of known physical quantities. For example, the function φ(r) is often represented in the form of one of the described above pair potentials or in the form of polynomials of the n-th order. The electron density n(r) if single atoms is described on the basis of quantum-mechanical approach. Finally, the information about the function f(ρ) can be obtained from the equation of state.

As the pair part, the authors of [16] used a polynomial dependence:

$$\varphi(r) = \begin{cases} 0, & r \geq r_c \\ \left(\frac{1}{a_1 r^2} - a_2\right)(a_1 r^2 - a_1 r_c{}^2)^{10}[(a_1 r^2 - a_1 r_c{}^2)^6 + a_3(a_1 r^2)^6], & r < r_c \end{cases} \quad \text{(a2.2a)}$$

The following analytical expressions were suggested for the embedding function and single-electron density:

$$f(\rho) = \frac{b_1 \rho \cdot [b_2 + (b_3 + \rho)^2]}{1 + b_4 \rho}, \qquad n(r) = \begin{cases} 0, & r \geq r_c \\ \frac{c_1 \cdot (r^2 - r_c{}^2)^2}{1 + (c_2 r^2)^3}, & r < r_c \end{cases} \quad \text{(a2.2a)}$$

Here r_c=0.6875 nm is the cutoff radius of the potential. The authors performed the parameterization of this potential using the minimization of total deviations of the components of the cold pressure tensor and experimental properties of Aluminum at low temperatures. Also, during minimization the following reference point had high weight: at the temperature T=0K the lattice constant of aluminum is a_0 = 0.4032 nm, the cohesion energy E_c = –324.19 kJ/mole and bulk modulus K = 80.9 GPa. As a result, the following values of the parameters were suggested, which are given in Table 2.

a_1	2.9275228176598036
a_2	5.1028014804162156
a_3	111.37742236893590

b_1	8.1106000931637006
b_2	-334.57493744623503
b_3	14.868297626731845
b_4	1.6080953931773090

c_1	0.58002942432410864
c_2	8.2981185422063639

Table 2. Parameters of EAM potential.

Thus, the parameterization of this potential was performed on the basis of the mechanical characteristics of aluminum. For the considered interatomic potential, the critical temperature is T_C = 7600 K, the critical pressure is P_C = 1400 bar, and the critical density is ρ_C = 0.5 g cm^{-3} [29]. Additional calculation details are presented in [30].

APPENDIX 3. COMPARISON OF TEMPERATURE AND DENSITY DISTRIBUTIONS ALONG *Z* AND *Y* DIRECTIONS.

In one-dimensional approximation used here for electron temperature heat diffusion is taken into account only in Z direction. The approximation validity usually does not raise doubts for sufficiently homogeneous condense matter state and large laser irradiation spot. However, it is not evident in the case of strongly inhomogeneous ablation plume region where density and temperature space variation are not small in all directions. For this region the approximation can be hardly justified but its effect on the temperature distribution and recoil pressure behavior in condensed matter seems to be not very significant.

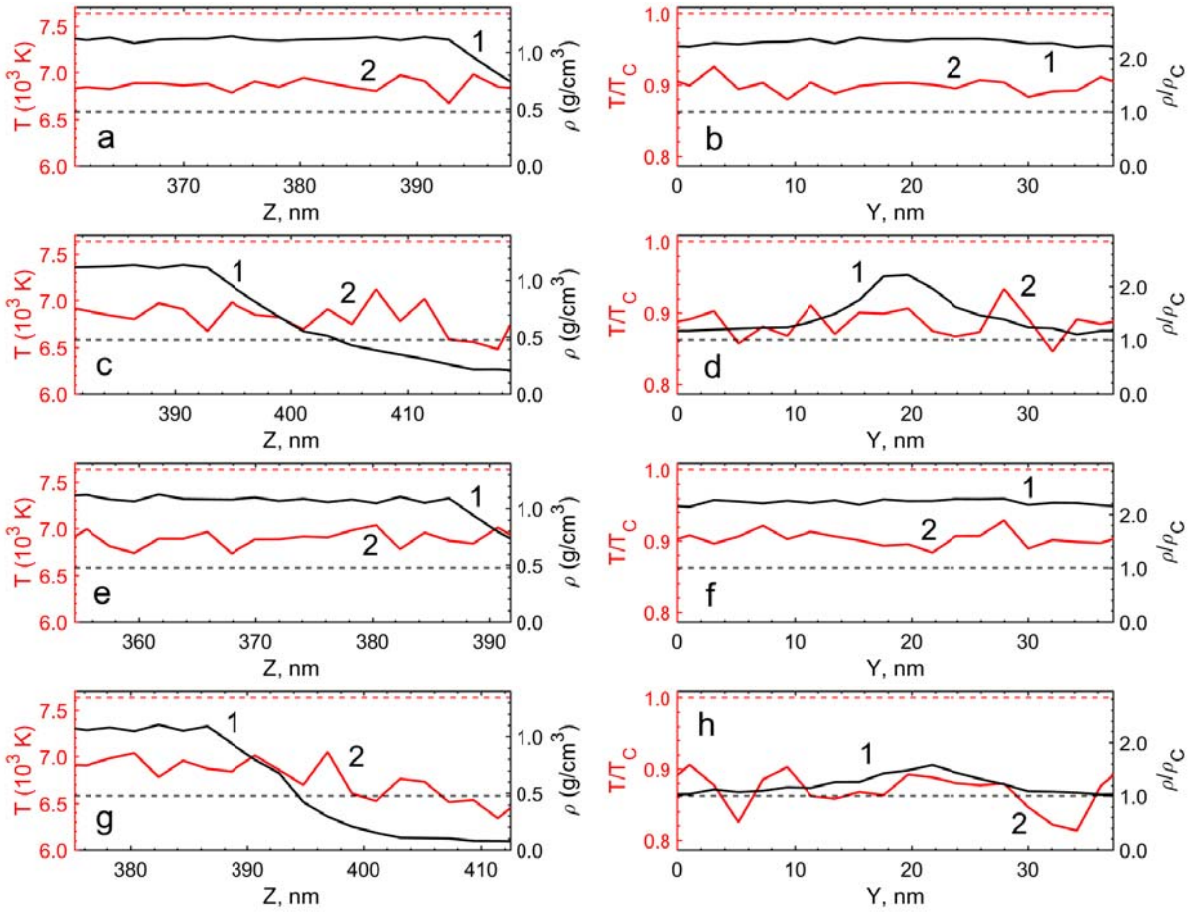

Fig.a3. The density (1) and temperature (2) distributions along Z (a, c, e, g) and Y (b, d, f, h) directions for different times 1905 ps (a-d) and 2070 ps (e-h). For further details see the text below.

At fig. a3(a-h) for the case $I = 33$ MW/cm^2 it is shown density (curves 1) and temperature (curves 2) distributions along Z (a, c, e, g) and Y (b, d, f, h) directions in subsurface area (a, b, e, f) and above it (c, d, g, h) with corresponding displacement 21 nm into the region where ablation plume formation begins. The curves a-d and e-h correspond to different times 1905 ps and 2070 ps during the first explosive boiling before and after maximum pressure peak which is shown in fig. 1a (curve 1).

In the curves, construction of the averaging procedure over some volumes in the form of plates is used. In appendix 1 (fig.a1) two examples of such volumes ($\Delta X \times \Delta Y \times \Delta Z$ = 37.3×37.3×2.1 nm^3 on the left of fig.a1 and 37.3×2.1×37.3 nm^3 on its right) are shown and each of them corresponds to one point on density and temperature curves in fig. a3 along Z and Y directions. Summations of the plate volumes along Z (left case) and along Y (right case) gives the total volume L_0^3.

One can see from fig. a3 that there is no pronounced difference between curves describing subsurface temperature distribution along Z direction (a, e) where electron thermal conduction is taken into account and Y direction (b, f) with no such conduction. It is clear that taking into account additional electron heat conduction in Y direction can hardly change the picture.

In the ablation plume region difference between temperature variations along Z direction (c, g) and Y direction (d, h) are somewhat more pronounced so that taking into account

electron thermal conduction along *Y* direction can give some effect on thermal equilibration and vaporization processes in the ablation plume. In fact in the plume already there is another 3D mechanism of heat exchange due to convection and evaporation-condensation processes provided with MD procedure which can be probably more important than additional electron heat conduction along *X*–*Y* directions. We suggest that application of 1D approximation for electron heat conduction in our consideration does not distort significantly recoil pressure behavior as compared with the case of 3D electron heat conduction.

REFERENCES

[1] E.M. Apfelbaum and V.S. Vorob'ev, "The predictions of the critical point parameters for Al, Cu and W found from the correspondence between the critical point and unit compressibility line (Zeno line) positions", *Chem. Phys. Lett.*, **467**, 318 (2009). DOI: 10.1016/j.cplett.2008.11.060

[2] Pengfei Ji, Yuwen Zhang, "Melting and thermal ablation of a silver film induced by femtosecond laser heating: a multiscale modeling approach", *Appl. Phys.*, A **123**, 671 (2017). DOI: 10.1007/s00339-017-1269-7

[3] A.L. Khomkin and A.S. Shumikhin, "Critical Points of Metal Vapors", *Journal of Experimental and Theoretical Physics*, **121**(3), 521–528 (2015). DOI: doi.org/10.1134/S1063776115090162

[4] D.S. Ivanov and L.V. Zhigilei. "Combined atomistic-continuum modeling of short-pulse laser melting and disintegration of metal films", *Physical Review B*, **68**, 064114 (2003). DOI: 10.1103/PhysRevB.68.064114

[5] V.I. Mazhukin, A.V. Shapranov, M.M. Demin, A.A. Samokhin, A.E. Zubko, "Molecular dynamics modelling of nanosecond laser ablation: subcritical regime", *Mathematica Montisnigri*, **37**, 24–42 (2016)

[6] V.I. Mazhukin, A.V. Shapranov, M.M. Demin, A.A. Samokhin, A.E. Zubko, "Molecular dynamics modelling of nanosecond laser ablation: transcritical regime", *Mathematica Montisnigri*, **38**, 78–88 (2017)

[7] A.A. Samokhin, V.I. Mazhukin, M.M. Demin, A.V. Shapranov, A.E. Zubko, "Molecular dynamics simulation of Al explosive boiling and transcritical regimes in nanosecond laser ablation", *COLA 2017, The 14th International Conference on Laser Ablation*, 185 (2017)

[8] V.I. Mazhukin, A.A. Samokhin, M.M. Demin, A.V. Shapranov. "Modeling of nanosecond laser vaporization and explosive boiling of metals", *Mathematica Montisnigri*, **29**, 68-90 (2014)

[9] M.I. Kaganov, I.M. Lifshitz, L.V. Tanatarov, "Relaxation between electrons and the crystalline lattice", *Journal of Experimental and Theoretical Physics*, **4**(2), 173-178 (1957)

[10] I.M. Lifshitz, M.I. Kaganov, L.V. Tanatarov, "K teorii radiacionnyh izmenenij v metallah", *At. Energ.*, **6**, 391-402 (1959)

[11] S.I. Anisimov, B.L. Kapeliovich, T.L. Perelman, "Electron emission from metal surfaces exposed to ultrashort laser pulses", *Sov. Phys. Journal of Experimental and Theoretical Physics*, **39**(2), 375-377 (1974)

[12] L.D. Landau, E.M. Lifshitz, *Statistical Physics*, Butterworth-Heinemann, Vol. 5 (3rd ed.), (1980)

[13] G.V. Gordeev, "Low-frequency plasma vibrations", *Journal of Experimental and Theoretical Physics*, **27**, 19-23 (1954)

[14] A.A. Ionin, S.I. Kudryashov, A.A. Samokhin, "Material surface ablation produced by ultrashort laser pulses", *Phys. Usp.*, **60**(2), 159–172 (2017). DOI: 10.3367/UFNe.2016.09.037974

[15] V.I. Mazhukin, "Kinetics and Dynamics of Phase Transformations in Metals Under Action of Ultra-Short High-Power Laser Pulses", Chapter 8, In "*Laser Pulses – Theory, Technology, and Applications*", InTech., ed. by I. Peshko., 219-276 (2012). DOI: 10.5772/50731

[16] V.V. Zhakhovskii, N.A. Inogamov, Yu.V. Petrov, S.I. Ashitkov, K. Nishihara, "Molecular dynamics simulation of femtosecond ablation and spallation with different interatomic potentials", *Appl. Surf. Sci.*, **255**, 9592 (2009). DOI: 10.1016/j.apsusc.2009.04.082

[17] I.N. Kartashov, A.A. Samokhin, I.Yu. Smurov, "Boundary conditions and evaporation front instabilities", *J. Phys. D: Appl. Phys.*, **38**, 3703–3714 (2005). DOI: 10.1088/0022-3727/38/19/020
[18] R.V. Karapetyan and A.A. Samokhin, "Influence of an increase in the transparency on the intense evaporation of metals by optical radiation", *Sov. J. Quant. Electron.*, **4**(9), 1141-1142 (1975). DOI: 10.1070/QE1975v004n09ABEH011557
[19] A.A. Samokhin, "First-order phase transitions induced by laser radiation in absorbing condensed matter", *Effect of laser radiation on absorbing condensed matter*, Nova Science Publishers, ed. by V.B. Fedorov, (1990)
[20] V.I. Mazhukin, A.A. Samarskii, "Mathematical modeling in the technology of laser treatments of materials", *Surveys on Mathematics for Industry*, **4** (85), 149 (1994)
[21] V.I. Mazhukin, V.V. Nossov, I. Smurov, "Analysis of laser-induced evaporation of Al target under conditions of vapour plasma formation", *Thin Solid Films*, **453 –454,** 353 (2004)
[22] V.I. Mazhukin, V.V. Nossov, I. Smurov, "Modeling of plasma-controlled evaporation and surface condensation of Al induced by 1.06 and 0.248 μ m laser radiations", *Journal of Applied Physics*, **101** (2), 024922 (2007). DOI: 10.1063/1.2431951
[23] A.A. Samokhin, N.N. Il'ichev, "On photoacoustic monitoring of laser evaporation front movement", *Quantum Electron*. **40**(8), 659–660 (2010). DOI: 10.1070/QE2010v040n08ABEH014382
[24] A.A. Samokhin, A.E. Zubko, "Application of intensity modulated nanosecond laser pulses for acoustical monitoring of metal ablation", *COLA 2017, The 14th International Conference on Laser Ablation*, 186 (2017)
[25] H.J.C. Berendsen., J.P.M. Postma, W.F. van Gunsteren, A. DiNola, J.R. Haak. "Molecular dynamics with coupling to an external bath", *J. Chem. Phys.*, **81**, 3684-3690, (1984)
[26] M.P. Allen and D.J. Tildesley, *Computer Simulation of Liquids*, Oxford: Clarendon Press, (2002)
[27] M.S. Daw and M.I. Baskes, "Embedded-atom method: Derivation and application to impurities and other defects in metals", *Phys. Rev. B*, **29**, 6443 (1984). DOI: 10.1103/PhysRevB.29.6443
[28] S.M. Foiles, M.I. Baskes, and M.S. Daw, "Embedded-atom-method functions for the fcc metals Cu, Ag, Au, Ni, Pd, Pt, and their alloys". *Phys. Rev. B*, **33**, 7983 (1986). DOI: 10.1103/PhysRevB.33.7983
[29] V.I. Mazhukin, A.A. Samokhin, A.V. Shapranov and M.M. Demin. "Modeling of thin film explosive boiling—surface evaporation and electron thermal conductivity effect", *Mater. Res. Express*, **2**, 016402 (2015) DOI: 10.1088/2053-1591/2/1/016402
[30] V.I. Mazhukin, A.V. Shapranov, O.N. Koroleva, A.V. Rudenko. "Molecular dynamics simulation of critical point parameters for silicon", *Mathematica Montisnigri*, **31**, 64 – 77 (2014)

Received December 10, 2017